Pertanika J. Sci. & Technol. 30 (2): 1689 - 1716 (2022)

PERTANIKA JOURNALS

SCIENCE & TECHNOLOGY

Journal homepage: http://www.pertanika.upm.edu.my/

The Effects of the Indonesian Throughflow, River, and Tide on Physical and Hydrodynamic Conditions During the Wind-Driven Upwelling Period North of the Aru Islands

Abdul Basit[1]*, Bernhard Mayer[2] and Thomas Pohlmann[2]

[1]National Research and Innovation Agency Republic of Indonesia, Centre for Deep Sea Research, Jl. Y. Syaranamual Guru-guru Poka, 97233 Ambon, Indonesia
[2]University of Hamburg Institute of Oceanography, Bundesstraße 53, 20146 Hamburg, Germany

ABSTRACT

A three-dimensional baroclinic nonlinear numerical model—the Hamburg Shelf Ocean Model (HAMSOM)—was applied to investigate the effects of the Indonesian throughflow (ITF), river runoff, and tidal forcing on circulation during the southeast monsoon period (July 2004) north of the Aru Islands by conducting different sensitivity runs. It was found that the Ekman transport over the continental slope of the Sahul Shelf was the main factor that causes upwelling north of the Aru Islands, and this was suggested to be one of the main factors behind the surface water in the research area being relatively colder and saltier than the surrounding waters. The influence of South Pacific Subtropical Water (SPSW) on the surface water was indicated by the high surface salinity of waters within the internal salinity maximum layer. The results also suggested that onshore subsurface currents over the slope were induced not only by offshore surface currents over the slope but also by the ITF. By considering the eastern ITF route, river runoff and tidal forcing were also found to contribute significantly to the erosion of the salinity maximum (approx. 0.25) within the Halmahera Sea, thereby reducing sea surface salinity north of the Aru Islands. Furthermore, it was proposed that river runoff from the western coast of Papua Island contributed to intensified cross-shelf circulation over the continental slope. These conditions were related to enhancing vertical viscosity forces in the surface waters induced by stronger stratification as an impact of river inclusion in the simulation.

Keywords: Aru Islands, river, tide, upwelling, wind

ARTICLE INFO

Article history:
Received: 21 October 2021
Accepted: 10 January 2022
Published: 31 March 2022

DOI: https://doi.org/10.47836/pjst.30.2.45

E-mail addresses:
abdul.basit1@my.jcu.edu.au (Abdul Basit)
bernhard.mayer@uni-hamburg.de (Bernhard Mayer)
thomas.pohlmann@uni-hamburg.de (Thomas Pohlmann)
*Corresponding author

ISSN: 0128-7680
e-ISSN: 2231-8526

INTRODUCTION

The Aru Islands are located in the northern Arafura Sea, a semi-enclosed sea in the eastern-most part of the Indonesian Archipelago, and separate the Sahul Continental Shelf from the Aru Basin (Figure 1). The continental shelf connecting the Aru Basin with the northern Sahul Continental Shelf plays an important role in inducing upwelling. Due to these conditions, the Banda and Arafura Seas (BAS) have high productivity levels and marine biodiversity, including an abundance of fish. In-situ observations found that primary production varies between 0.91 $gC/m^2/d$ (during the northwest monsoon) and 1.85 $gC/m^2/d$ (during the southeast monsoon) (Gieskes et al., 1990). From satellite-derived observations (Figure 2a), it was clear that the chlorophyll-a concentration during the southeast monsoon (July 2004) was higher around the BAS than in the surrounding area; this confirmed the findings of Ilahude et al. (1990) and Wetsteyn et al. (1990). Upwelling was also indicated by the sea surface temperature (SST) being relatively lower around the BAS than in the surrounding area (Figure 2b), confirming the findings of Wyrtki (1961), Zijlstra et al. (1990), and Kida and Richards (2009). These tendencies suggest the occurrence of wind-driven upwelling around the BAS when southeasterly winds blow over the Northern Arafura Sea (Appendix - Figure A1).

In the Indonesian seas, water masses within the internal salinity maximum layer (depths of 50–300 m) were strongly influenced by the water that flows from the Pacific Ocean into the Indian Ocean through the Indonesian throughflow (ITF) (Wyrtki, 1961; Gordon, 2005; Koch-Larrouy et al., 2007; Gordon et al., 2008; Gordon et al., 2010; Mayer et al., 2010; Sprintall et al., 2014; Sprintall et al., 2019). They found that around 90% of the water mass constituted North Pacific Subtropical Water (NPSW), which was transported through the Sulawesi Sea and the Makassar Strait (collectively termed the western route) before entering the Banda Sea, Northern Arafura Sea, then exiting into the Indian Ocean through the Ombai Strait and Timor Passage (Gordon, 2005; Gordon et al., 2010; Mayer et al., 2010; Sprintall et al., 2014; Sprintall et al., 2019). The remaining water mass (10%), which constituted SPSW, was suggested to be transported partly through the Halmahera and Seram Seas (collectively termed the eastern route) before entering the northern Arafura and Banda Seas (Sprintall et al., 2014; Sprintall et al., 2019). They also suggested that some were transported through the Maluku Sea and Lifamatola before entering the Banda Sea. The eastern route is still uncertain. However, SPSW could be distinguished from NPSW by its higher salinity maximum; the former was generally identified by a salinity maximum of > 34.8, while the latter was generally identified by a salinity maximum of 34.4 and 34.8 (Wyrtki, 1961). The temperature was also found to be characteristic; SPSW was relatively warmer than the NPSW. As a consequence of the eastern route, the salinity maxima in the eastern Indonesian Seas were generally higher than in the western Indonesian Sea (Wyrtki, 1961; Gordon et al., 1994; Koch-Larrouy et al., 2007).

Due to the highly variable bathymetry of the Indonesian Seas (Figure 1), tidal interactions with the bottom topography have been found to contribute significantly to physical and hydrodynamic conditions. In a simulation, it was found that internal tide generated a colder SST (Koch-Larrouy et al., 2007; Nugroho et al., 2018). Therefore, tidal mixing was suggested as the most important mechanism in inducing a lower SST. In the Eastern Indonesian Seas (EIS), tidal mixing is confined around the Halmahera and Seram Seas, where shallow sills and narrow straits are located (Koch-Larrouy et al., 2007; Koch-Larrouy et al., 2015; Nagai & Hibiya, 2015; Nagai et al., 2017; Nagai et al., 2021; Ray & Susanto, 2016). Consequently, salinity within the internal salinity maximum layer was also reduced. Considering the role of the northern Arafura Sea in the eastern ITF and highly variable bathymetry of the Sahul Shelf around the Aru Islands (Appendix—Figure A1), numerical simulations that consider tidal forcing was deemed necessary to obtain better estimates and deeper understandings of the physical processes around the Aru Basin.

River runoff also has been found to significantly influence the physical and hydrodynamic properties of water in the Arafura Sea. More than thirty rivers flow southwest from Papua Island into the Arafura Sea (Alongi et al., 2011). It was estimated that river runoff along the western coast of the Papua Island varied between 11,088 m^3/s and 13,747 m^3/s during the southeast monsoon season averaging 25 years of simulation data from 1990 through 2014 (Basit, 2019). Zijlstra et al. (1990) found that river runoff contributes primarily to the salinity field, rather than the nutrient budget, of offshore waters. Wind-driven upwelling, meanwhile, was deemed the main mechanism responsible for the relatively high nutrient concentration of the upper water column during the southeast monsoon (Ilahude et al., 1990; Wetsteyn et al., 1990; Zijlstra et al., 1990; Kämpf, 2016). Nonetheless, river runoff could also have a significant effect on a circulation, as suggested by Allen et al. (1995), Lentz (2001), and Gan et al. (2009). Enhanced vertical stratification, induced by surface freshwater, could reduce the depth of the mixed layer and subsequently enhance the efficiency with which wind forcing induces cross-shelf circulation (Allen et al., 1995; Lentz, 2001; Gan et al., 2009).

This research aimed to investigate the effects of the ITF, river runoff, and tidal forcing on circulation north of the Aru Islands, which are located at the northern Arafura Sea, during the southeast monsoon period (July 2004), during a period when influences of the Indian Ocean Dipole (IOD) and the El Niño/Southern Oscillation (ENSO) were relatively weak (https://psl.noaa.gov/gcos_wgsp/Timeseries/DMI/ and https://origin.cpc.ncep.noaa.gov/products/analysis_monitoring/ensostuff/ONI_v5.php) and more observation data could be used for model validation. Following this introduction, this paper describes the material and methods. The simulation results, including validation, sensitivity experiments for different forcing fields, and momentum analyses, are presented and discussed in the following section. Finally, a conclusion is provided in the last section.

MATERIAL AND METHODS

Model Design

This investigation employed the Hamburg Shelf Ocean Model (HAMSOM) designed by Backhaus (1985), Pohlmann (1996a, 1996b, 2006), and their colleagues. The bathymetry was generated from a 30-second resolution grid of Shuttle Radar Topography Mission (SRTM), linearly interpolated to obtain a 3-minute resolution bathymetry for the regional model. The model domain ranged from 114°E to 139°E and from 14°S to 12°N (Figure 1), covering the ITF transport region from the Western Pacific Ocean to the Banda and Arafura Seas. Initial and open boundary conditions were provided by the Max-Planck-Institute Global Ocean/Sea Ice Model (MPI-OM) (Marsland et al., 2003; Jungclaus et al., 2006) with a 24 min horizontal resolution and 40 vertical layers. Initial and open boundary conditions, including T, S, current, and SSH, were interpolated to the regional model grid with 54 vertical layers. The vertical layer thickness was smallest near the surface, increasing gradually towards the bottom to better represent the mixed and internal salinity maximum layers.

A Smagorinsky scheme was implemented to calculate the non-constant coefficients of horizontal viscosity, which depended on the horizontal shear stress to parameterize the horizontal sub-grid-scale dynamical processes. The Smagorinsky Equation 1 is as below.

$$A_h = c.dx.dy.\sqrt{\frac{\partial u}{\partial x}^2 + \frac{1}{2}\left(\frac{\partial v}{\partial x} + \frac{\partial u}{\partial y}\right)^2 + \left(\frac{\partial v}{\partial y}\right)^2} \quad (1)$$

was provided, with c being a dimensionless coefficient set to 0.5 for the simulations, u and v represent zonal and meridional velocities in m/s.

The vertical turbulent viscosity coefficient was calculated by applying the approach of Kochergin (1987) as implemented by Pohlmann (1996b). He estimated that the coefficient was directly proportional to the square root of the vertical density gradient and the vertical shear stress (Equation 2).

$$A_v = (c_{ML}.h_{ML})^2.\sqrt{\left(\frac{\partial u}{\partial z}\right)^2 + \left(\frac{\partial v}{\partial z}\right)^2 + \frac{1}{S_M}\frac{g}{\rho}\frac{\partial \rho}{\partial z}} \quad (2)$$

where Kochergin's constant (c_{ML}) was estimated by 0.05, h_{ML} was the turbulent mixed layer depth at the surface and the bottom, and S_M was the Prandtl number. The Richardson number determines the depth of the turbulent mixed layer.

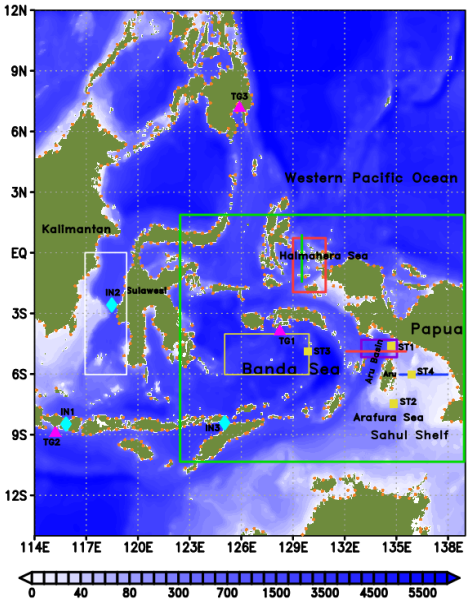

Figure 1. Topography of the model area in meters. The green rectangle and the red line (Section A) delineate the specified regions discussed mostly in this paper. The solid orange circles along the coastline represent the river locations; the purple triangles indicate the locations of the tide gauge stations (TG1: Ambon, TG2: Benoa, TG3: Davau). The solid light-blue diamonds represent INSTANT stations (IN1: Lombok Strait, IN2: Makassar Strait, IN3: Ombai Strait). The solid yellow squares represent validated SST locations (ST1: North of Aru Islands, ST2: Southern Aru Islands, ST3: Banda Sea; ST4: Sahul Shelf). The red (in the Halmahera Sea), yellow (in the Banda Sea), white (in the Makassar Strait), and purple (in the northern Arafura Sea) rectangles indicate the regions where the T-S diagrams were plotted. The green (Section B) and yellow lines (Section C) delineate the region where the vertical turbulent viscosity coefficients were taken as samples for comparison between the WRT and WR cases.

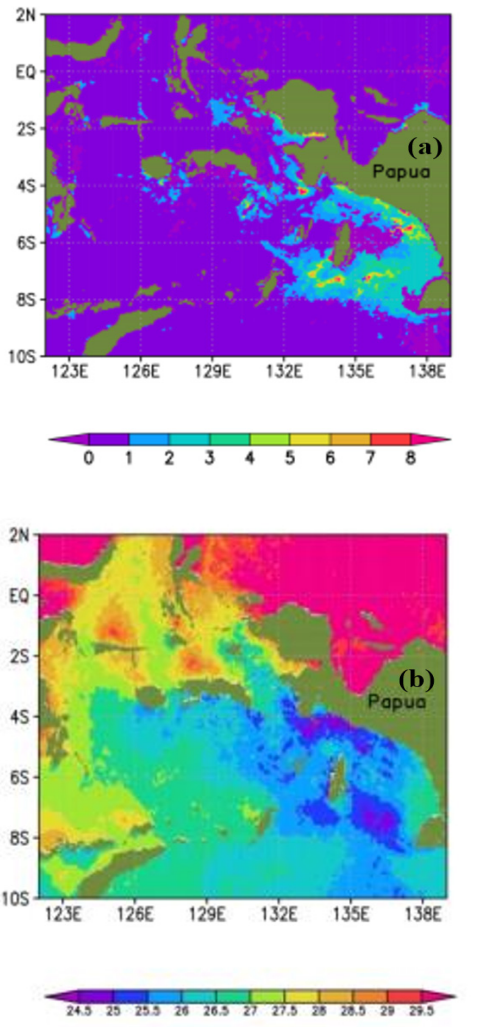

Figure 2. Horizontal distributions of chlorophyll-a (gC/m^2) (a) and SST (°C) (b) derived from MODIS with the horizontal resolution of 5.5 x 5.5 km (http://icdc.cen.uni-hamburg.de), monthly averaged during the southeast monsoon (July 2004) around the Banda and Arafura Seas.

Model Forcing

The fluxes of momentum, heat, and freshwater at the sea surface were determined by means of bulk formulae. Atmospheric forcing, including atmospheric sea surface pressure, air temperature, specific humidity, u-wind, v-wind, and precipitation rate, were derived from the National Center for Environmental Prediction (NCEP) (Kalnay et al., 1996). Daily river discharge was obtained from the WaterGAP Global Hydrology Model (WHHM)

(Döll et al., 2003). The model also included tidal forcing along the open ocean boundary, with eleven tidal components (M2, S2, K1, O1, Q1, P1, N2, K2, M4, MS4, Mn4) derived from TPXO.6.2 (Egbert et al., 1994; Egbert & Erofeeva, 2002).

Numerical Experiments

In addition to the simulation with full model forcing, three additional experiments (Table 1) were performed for 2004 to investigate the influence of river runoff and tidal forcing on hydrodynamic conditions during the southeast monsoon when upwelling occurred. These three additional experiments were conducted by excluding river discharge (WT), excluding tidal forcing (WR), and excluding both (WO). Results were compared with the control run (WRT), which includes all three forcing components: wind, river discharge, and wind. In addition, spin-up was performed by running all experiments for the two years (from 2002 to 2003) before the investigation period.

Table 1
Numerical experiment design

No	Experiments	Wind	River runoff	Tidal elevation
1	Control run (WRT)	Y	Y	Y
2	No-River (WT)	Y	N	Y
3	No-Tide (WR)	Y	Y	N
4	Wind only (WO)	Y	N	N

RESULTS AND DISCUSSIONS

Model Validation

Tidal Elevations. The HAMSOM regional model was generally able to simulate the time series of tidal elevations in the model area reasonably well (Figure 3). The evaluation was conducted for selected areas by comparing the HAMSOM results with in-situ data taken from the University of Hawaii Sea Level Center (Caldwell et al., 2015). A strong correlation was found between the modeled and observed tides, as indicated by a correlation coefficient (r) of 0.82–0.92. However, in the case of Ambon, the amplitude reproduced by the simulation tended to overestimate the observational data, with a root-mean-square deviation (rmsd) of 0.31 m (higher than in other locations). It was thus suggested that the model could not resolve the specific conditions of the Ambon tide gauge station. The gauge station is located in the Inner Ambon Bay, separated by narrow and shallow channels that are approximately 800 m wide and less than 50 m deep; a model with a resolution of 3’ (approx. 5 km) was insufficient to resolve such special conditions adequately.

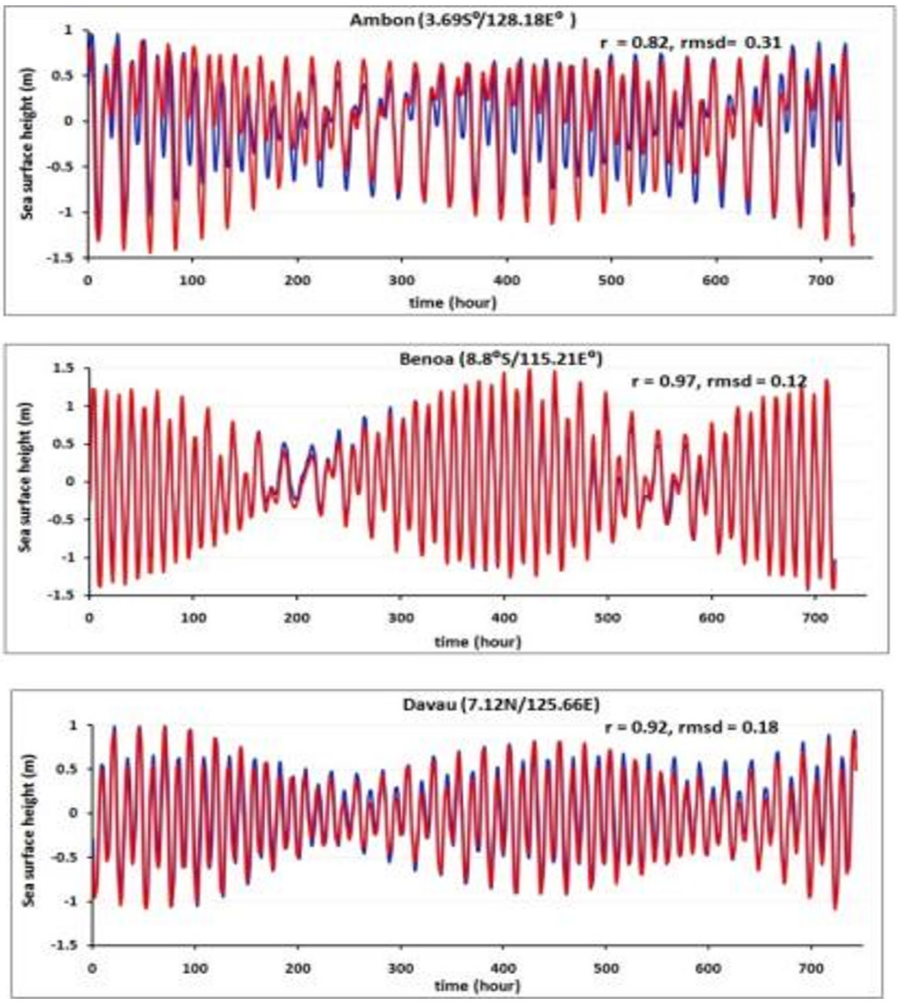

Figure 3. Time series of measured (blue lines) and simulated (red lines) sea surface heights in selected points (see also in Figure 1), i.e., a) Ambon (TG1, July 2004); b) Benoa (TG2, September 2004); c) Davau (TG3, July 2004).

Sea Surface Temperature (SST)

The simulated monthly average SST was generally in good agreement with the SST products from the MODIS (Figure 4). In addition, seasonal patterns were shown, with relatively low temperatures of 24–25˚C between July and August (during the southeast monsoon) and relatively high temperatures of 30–31˚C between January and February (during the northwest monsoon). Over twelve years (between 2003 and 2014), a good correlation, with the correlation coefficient (r) of between 0.82 and 0.97, was indicated between the simulated and measured data in the Banda and northern Arafura Seas (from 130° E–137° E and from 4°S to 8°S). However, the simulated maximum and minimum temperatures

were generally lower than those observed; peak temperatures were particularly vulnerable to underestimation. Therefore, it was attributed to the model; for HAMSOM, SST was drawn from the upper-temperature layer (with a thickness of 5 meters), while the observed SST was valid for the upper few centimeters.

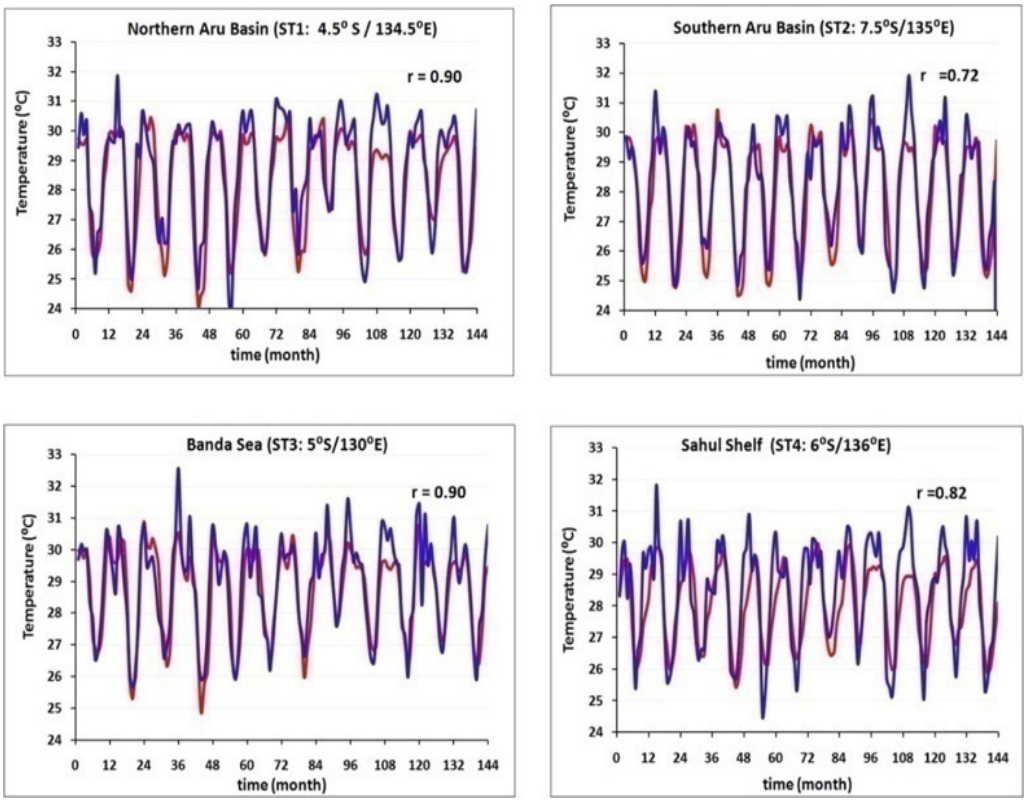

Figure 4. The values of SST from MODIS (blue color) and the HAMSOM simulation (red color) in the 2003–2014 period in the Banda and northern Arafura Seas (in the northern and southern of Aru Basin and Sahul Shelf in selected points (see also Figure 1).

Meridional Velocities. Meridional velocities were verified at three locations: the Makassar Strait (2.86˚S/118.45˚W), the Lombok Strait (8.4˚S/115.9˚W), and the Ombai Strait (8.53˚S/125˚W) (Figure 5). The Makassar Strait is the main inflow passage of the ITF, where water masses from the northwest Pacific Ocean enter the Indonesian Seas, while the other straits are exit gates through which Indonesian water masses exit into the Indian Ocean. Measured data were obtained from the International Nusantara Stratification and Transport (INSTANT) project (Sprintall et al., 2004). The simulation results generally showed acceptable agreement with the observational data, as indicated by the correlation coefficient (r), which varied between 0.49 and 0.75.

However, the correlation for velocity was lower than for SST. It may be attributed to differences in measurement; velocity was observed in specific locations and depths, while the model interpreted the mean velocity of a particular model grid cell covering a defined depth range. Conversely, both the simulated SST and the MODIS SST interpreted the mean SST of a specific model grid cell (21 km^2 and 30 km^2 in size), and thus correlation was higher. Depth was also found to contribute to correlation. For example, at depths of 50 m and 150 m, the corresponding layer thicknesses were 7 m and 22 m, respectively; consequently, the correlation was lower in deeper regions. However, the simulated velocities were still acceptable, as they mostly aligned with the observed velocities and were also able to produce low and high variations within the correct range.

In both the simulated (red line) and observational (blue line) data, the meridional currents in the two layers were generally directed southward. However, some northward currents were found, mostly during the transition periods of May/June and November/December. It was also observed that the current intensities in both the simulations and observational results follow seasonal variations. For example, in the Makassar Strait, current intensities in the upper and lower layers were generally higher in the two data sets during the southeast monsoon (July–October) than during the northwest monsoon (December–February). It suggested that more water from the North Pacific Ocean entered the Indonesian Seas within the upper internal salinity maximum layer (50–150 m) during the southeast monsoon than during the northwest monsoon, as also observed by Gordon and Susanto (2008), and modeled by Mayer and Damm (2012). Similarly, in the two selected depth levels, the higher intensity was generally observed in the two exit gates (the Lombok and Ombai Straits) during the southeast monsoon than during the northwest monsoon; this holds for both the model and the observational data.

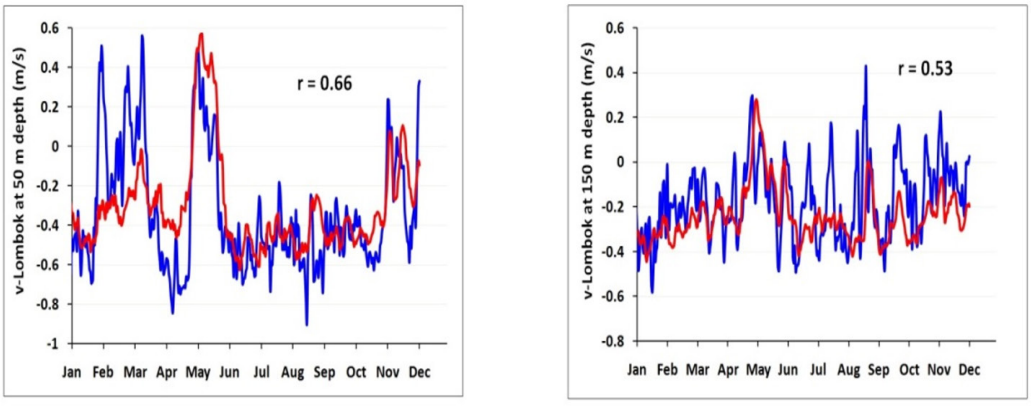

Figure 5. HAMSOM-simulated (red line) and INSTANT-observed (blue line) meridional velocities at a depth of 50 m (left) and 150 m (right) in the Lombok, Makassar, and Ombai Straits (IN1, IN2, IN3 in Figure 1) in the year of 2004.

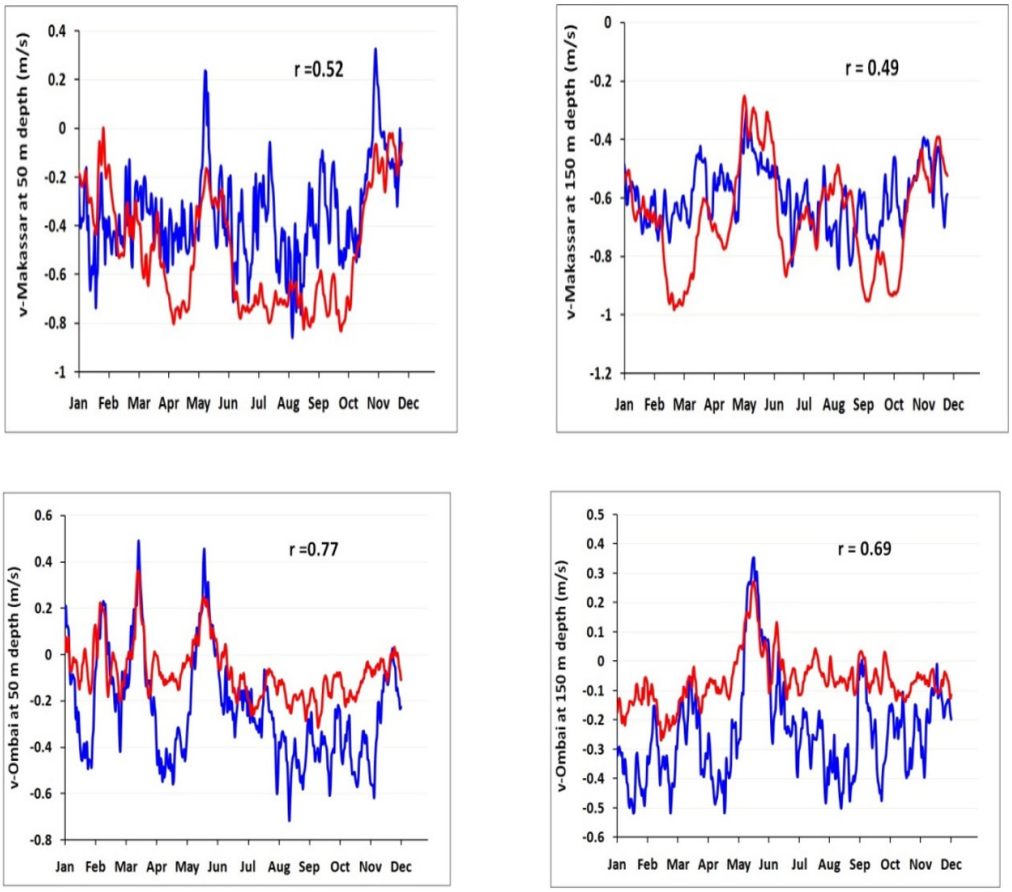

Figure 5. (Continue)

T-S Diagram. The results of the four simulation experiments—the WRT (red line), WO (yellow line), WR (blue line), and WT (green line) cases—were compared with observed EN4 data (cyan line), which was based on data taken from all instruments being able to profile the water column (Good et al., 2013) in the selected areas, i.e., the Halmahera Sea, Banda Sea, Makassar Strait, and the northern Arafura Sea (Figure 1) utilizing a T-S diagram for the year 2004 (Figure 6), were obtained via the Integrated Climate Data Center (https://icdc.cen.uni-hamburg.de/en/en4.html). The main data source for the data set of EN4 was the WOD09. The other data sources were also from data compiled during the Arctic Synoptic Basin Wide Oceanography (ASBO) project, the Global Temperature and Salinity Program (GTSPP), and the Argo global data assembly centers (GDACS) (Good et al., 2013).

In the WRT case, the simulated T-S diagram was shown to have a generally good agreement with observed data. In both areas, deviations between observed salinity and the WRT case were between 0.15 and 0.4. By excluding tidal forcing (the WR case), a significant deviation of about 0.4 and 0.7 was observed in the Halmahera Sea and the northern Arafura Sea, respectively, indicating that the exclusion of tidal forcing resulted in the overestimation of the salinity maximum. Considering the presence of sills and narrow straits in the Halmahera Sea (Figure 1), the eroded salinity maximum in the tidal inclusion simulations suggested that relatively strong internal tidal mixing around the Halmahera Sea enhanced vertical mixing around this area (Appendix—Figure A3). Figure A3 (Appendix) showed that the vertical turbulent viscosity coefficient within the water column at about 0.8° N was found relatively higher in the tide simulation (the WRT case) than in the no-tide simulation (the WR case).

As a consequence of this mixing, deeper waters with relatively low salinity and temperature were upwelled and mixed, reducing the salinity and temperature of the internal salinity maximum layer. Furthermore, the results suggested that the supply of low-salinity surface water played an important role in stabilizing the surface water, producing better results in the WRT case than in the WT case. More specifically, the mixing generated by tidal forcing and rough topography was suggested to reach the surface as found by Nugroho et al. (2018), thereby bringing relatively fresh water down to the subsurface and subsequently reducing the salinity of the internal salinity maximum layer. Comparing the WRT and WT cases, it was also shown that the significantly lower salinity maximum in the Halmahera Sea in the WRT case was accompanied by lower temperature; this suggested that stronger tidal mixing occurred in the WRT case, and thus more deep water with lower salinity and colder temperature intruded into the upper layers. This stronger tidal mixing may be caused by the eastern ITF inflow being weaker in the WRT case than in the WT case. Given the influence of the eastern ITF, this condition could induce lower SSS and lower SST north of the Aru Islands during the upwelling period, as discussed in the next section. In addition, it was found that relatively fresh surface water contributed relatively little to the reduction of subsurface salinity when tidal forcing was excluded from the simulation, as indicated by comparing the WO and WR cases. The T-S diagrams of both the WR and WO cases were similar in that their salinity maxima in the Halmahera Sea were overestimated by about 0.4.

In all simulations and global observation data, it was found that the salinity maximum was lower in the northern Arafura Sea (where the water originated mostly from the Halmahera Sea) than in the Halmahera Sea (Figure 6). Recognizing not only the tidal mixing between the Halmahera Sea and the northern Arafura Sea along the eastern ITF pathway but also the relatively lower salinity of water from the Banda Sea entering the Aru Basin that will be discussed in the next section (Figure 8b), this suggested that horizontal mixing occurred along the pathway and reduced the salinity maximum in the northern Arafura Sea.

The deviation of salinity maximum between the control run and observation in the Northern Arafura Sea was quite large (about 0.4), even though the WRT showed the smallest deviation. Therefore, the study suggested that the vertical turbulent coefficient below the surface layers applied in this simulation was quite small compared to the observation. For example, It was observed that the coefficient around the Halmahera Sea ranged between 9.1 x 10^{-5} and 1.6 x 10^{-3} m^2/s (Purwandana et al., 2020). Meanwhile, the coefficient applied in this simulation in this area varied between 8 x 10^{-6} and 5 x 10^{-4} (Appendix—Figure A3). Consequently, the salinity maxima produced by the simulation along the eastern ITF was relatively higher than in the observation. However, the simulation showed acceptable results because some simulation patterns were also found in the observation. For example, the results showed that the salinity maxima in the Halmahera Sea, Seram Sea, and Northern Arafura Sea were higher than in the Makassar Strait and the Banda Sea, as discussed in more detail in the following section (see also Figure 8). This pattern was also observed by Wyrtki 1961 (Plate 33).

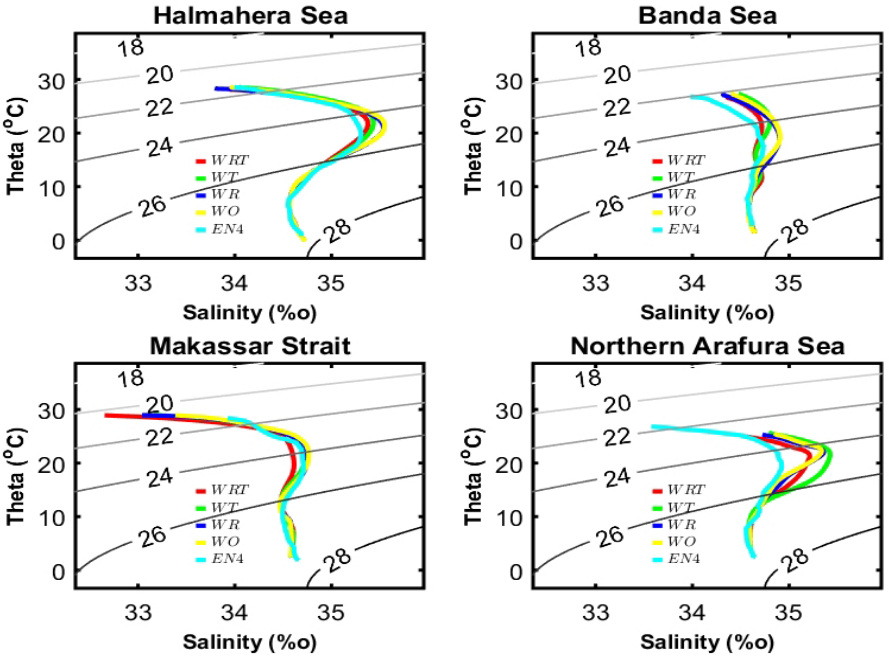

Figure 6. T-S diagram derived from HAMSOM simulations and observation data (EN4), monthly averaged for the July 2004 period in the selected areas, i.e., Halmahera Sea, Banda Sea, Makassar Strait) and Northern Arafura Seas (the WRT case (red), the WO case (yellow), the WR case (blue), the WT case (green), and measured data (cyan).

Sensitivity Studies

Reference Case. In the reference case (WRT), areas with relatively lower SST than in surrounding areas (indicating the center of upwelling) were visible around the north and south of Aru Islands (Figure 7), where southeasterly winds blow (Appendix—Figure A2). The investigation focused on the area north of the Aru Islands, where southeasterly winds were also observed to generate westward surface offshore currents. These surface currents induced upwelling and, with the continental slope, subsequently generated onshore subsurface currents that brought subsurface water with relatively low temperature and high salinity to the surface. Surface salinity and temperature around this area were found to reach approximately 35 and 25°C, respectively.

Additionally, the physical conditions of the surface water north of the Aru Islands were influenced by surface water from the Sahul Shelf located between the Aru and Papua Islands, which (due to river runoff along the western coast of Papua) was found to be relatively fresher and warmer. Meanwhile, water within the internal salinity maximum layer along the eastern ITF pathway (the Halmahera, Seram, and northern Arafura Seas) is relatively warmer and saltier than in the Banda Sea, indicating the influence of SPSW (Figure 8). This pattern was similar to the observation global data of EN4 (Appendix - Figure A4).

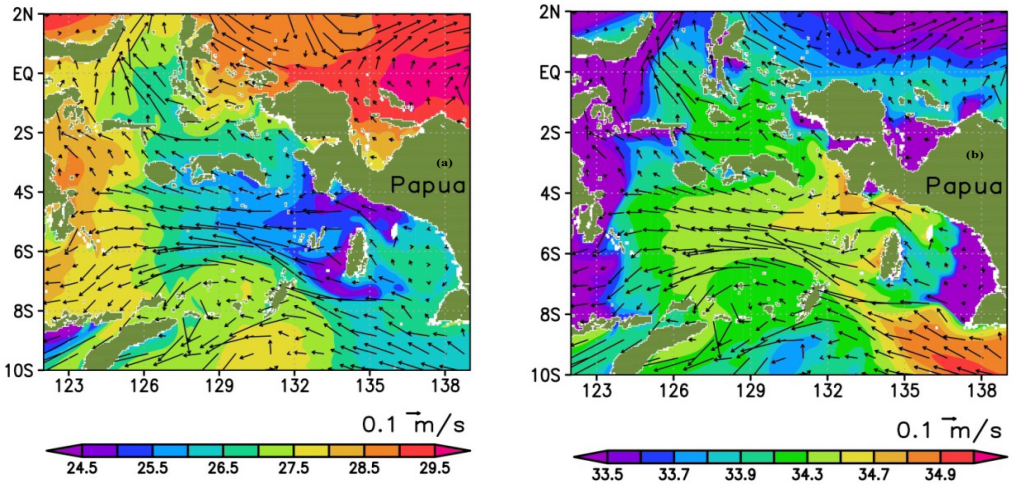

Figure 7. Monthly averages of SST (°C) (a) and SSS (b), overlaid by surface currents, in July 2004 (28 days), WRT case.

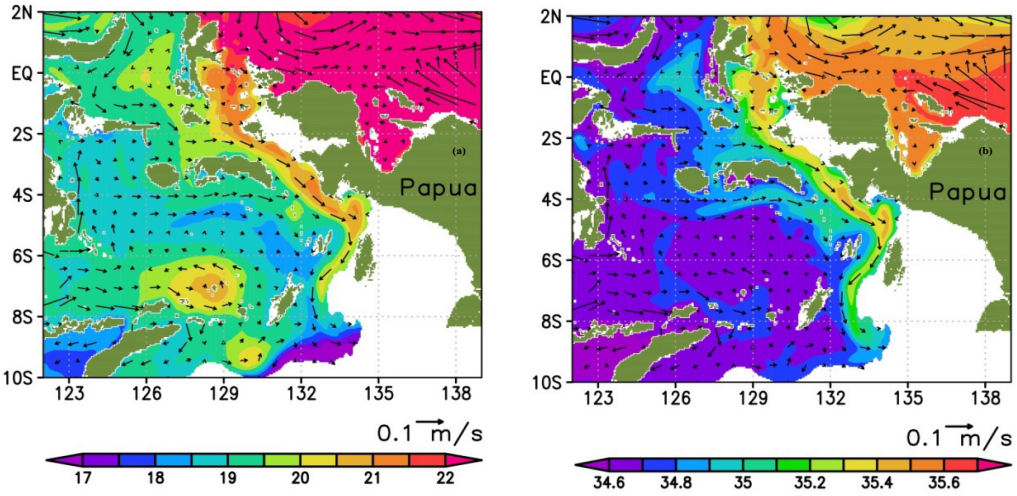

Figure 8. Monthly averages of subsurface temperature (°C) (a) and subsurface salinity (b) at a depth of 130 m, overlaid by surface currents, in July 2004 (28 days), WRT case.

In the vertical sections (Figures 9a and 10a, upper 350 m), upward-sloping isotherms and isohalines toward onshore over the Sahul Shelf Break were indicative of upwelling. A mixed layer could be detected down to a depth of about 50 m (with a temperature threshold of 0.5°C (Monterey & Levitus, 1997), with the internal salinity maximum layer found at depths of 50–300 m. The study suggested that this was attributed to the inflow of transformed SPSW. According to the model results, water entered the northern Arafura Sea through the Halmahera and Seram Seas (Figure 8), confirming the findings of Kämpf (2016), Atmadipoera et al. (2020), and subsurface currents velocities were highest at a depth of approx. 60 m (i.e., the upper internal salinity maximum layer; see Figure 9). This part of the ITF was found to intrude partly onto the continental slope north of the Aru Islands (Appendix—Figure A5), which suggested that the relatively strong onshore currents around the continental slope were induced not only by the Ekman surface currents but also by the intensity of the eastern ITF. These currents, carrying water masses with relatively high levels of salinity, were found to flow into the Sahul Shelf and strongly influence the surface waters in the area. Tidal mixing, induced by *the rough* topographic features of the Sahul Shelf (Appendix—Figure A1), was also prominent in this area and thus enhanced vertical mixing. Such enhanced vertical mixing was indicated by the vertical turbulent viscosity coefficient (Av) being relatively higher in the WRT case than in the simulation without tidal forcing (the WR case) (Appendix—Figure A6). Furthermore, it was found that the surface waters flow partly into the area north of the Aru Islands, indicating the influence of SPSW coming to the Sahul Shelf to the surface water of the area north of the Aru Islands (Figure 7). Observation of the vector uw-velocities, meanwhile, found that SPSW also influenced

the surface water in the northern Sahul Shelf (Figures 9a and 10a). Waters from the internal salinity maximum layer were found to move partly upward to reach the upper layer, and as a result, SSS was higher north of the Aru Islands than in surrounding areas (Figure 7b). Upwelling was further indicated by water density being relatively higher around the Sahul Shelf Break than in surrounding areas (Appendix—Figure A5).

Influence of River Runoff. River runoff along the western coast of Papua Island was estimated to be approx. 8353.203 m^3/s during the July 2004 period. By excluding river runoff from the simulation (WT case), SSS became higher (by about 0.1) than in the WRT case. Furthermore, SST north of the Aru Islands was relatively warmer in the WT case than in the WRT case (Figures 9a and b). In both the WRT and WT cases, temperatures at a depth of 50 m varied between 24˚C and 26˚C. However, in the WT case, water temperatures were generally higher than in the WRT case by about 0.5˚C; likewise, estimated water temperatures of 25–26˚C were more common at a depth of 50 m in the WT case than in the WRT case (where estimated water temperatures were mostly at 24–25˚C). This finding suggested that the lower SST in the WRT case could be attributed to cross-shelf circulation being stronger over the continental slope in the WRT case than in the WT case. As shown in Figures 9a and b, the vertical structure of the u-w velocity is similar in the WRT and WT cases. However, using momentum analysis (as discussed in Section 5), the stronger cross-shelf circulation of the WRT case could be more clearly identified, as the Coriolis term was higher in the WRT case. The different u-velocities of the WRT and WT cases can also be seen in Figure A7 (Appendix).

Higher salinity levels were detected within the upper internal salinity maximum layer (depths of 50–200 m) in the WT case than in the WRT case. Considering the eastern pathway of the ITF (Halmahera Sea-Seram Sea-Arafura Sea, Figure 8a), the lower salinity levels within the internal salinity maximum layer indicated that tidal mixing around the Halmahera Sea was relatively stronger in the WRT case. As a result, fresh surface water was drawn down to, and deep water was pulled up to the maximum internal salinity layer, eroding the salinity levels. It was illustrated by a T-S diagram comparing the WRT and WR cases (see Section TS-diagram). The occurrence of tidal mixing was also indicated by the vertical turbulent viscosity coefficient (Av) along section B of the Halmahera Sea being relatively higher in the WRT case than in the WR case (Figures 1 and Appendix—A3). The results also found that river runoff induced lower temperatures in the internal salinity maximum layers. In comparison to the observed data (EN4), it was found that the salinity maximum was overestimated in the Halmahera Sea in the WRT case by about 0.15. In contrast, in the WT case, the salinity maximum was overestimated by 0.4 (Figure 6). It suggested that, in addition to the river runoff along the western coast of Papua Island, the lower salinity of surface waters in the WRT case north of the Aru Islands was influenced by lower

salinity in the internal salinity maximum layer. In terms of temperature, meanwhile, the study suggested that the lower SST in the WRT case was determined not only by stronger upwelling but also by the entry of colder waters from the Halmahera Sea into the internal salinity maximum layer (see also section of TS-diagram).

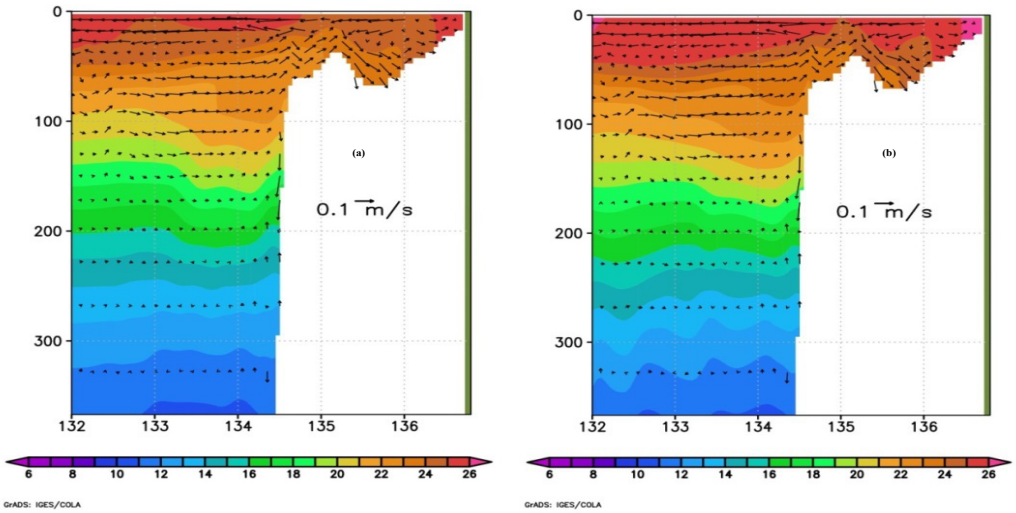

Figure 9. Vertical profiles of u-w velocity (u-velocity in m/s, w-velocity in x 10^{-3} m/s) and temperature (°C, shading) in Section A (4.8°S and 131°E–136°E), monthly averaged for the July 2004 period (28 days) in the a) WRT and b) WT cases.

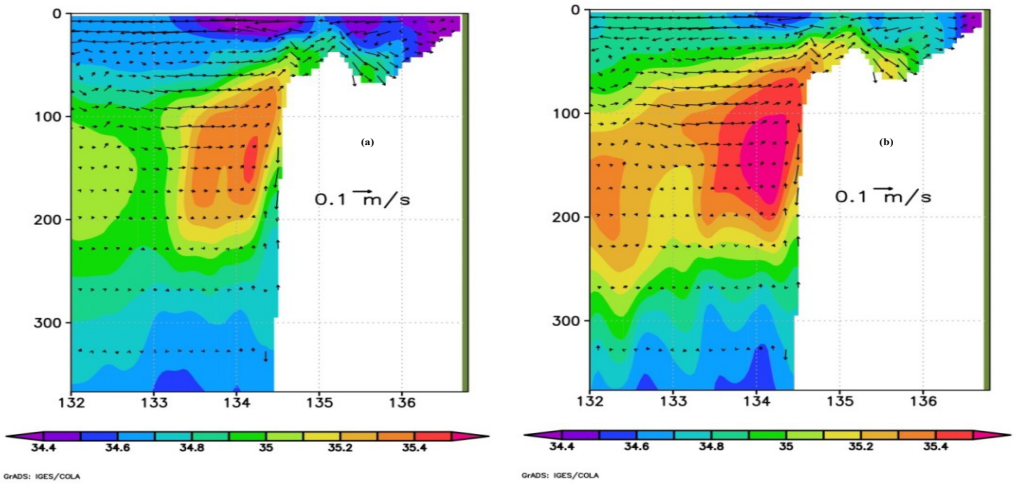

Figure 10. Vertical profiles of u-w velocity (u-velocity in m/s, w-velocity in x 10^{-3} m/s) and salinity (shading) in Section A (4.8°S and 131°E–136°E), monthly averaged for the July 2004 period (28 days) in the a) WRT and b) the WT cases.

Momentum Analysis

The 28-day (2 neap–spring cycles) mean of momentum components was calculated for the WRT and WT cases to explain the influence of rivers on hydrodynamic conditions during the wind-driven upwelling period (July 2004) north of the Aru Islands. Seven acceleration components were defined as Equation 3;

$$\overbrace{\frac{\partial \vec{U}}{\partial t}}^{ACCEL} + \overbrace{\vec{U} \cdot \nabla_h \vec{U}}^{HADV} + \overbrace{w \cdot \frac{\partial \vec{U}}{\partial z}}^{VADV} - \overbrace{2\Omega \times \vec{U}}^{COR} = \overbrace{-\frac{1}{\rho}\nabla P}^{PGA} + \overbrace{A_h \nabla^2 \vec{U}}^{HVI} + \overbrace{\frac{\partial}{\partial z}\left(A_v \frac{\partial \vec{U}}{\partial z}\right)}^{VVI} \quad (3)$$

where ACCEL: Local acceleration; HADV: Horizontal nonlinear advective acceleration; VADV: Vertical nonlinear advective acceleration; ADV = VADV + HADV; COR: Coriolis acceleration; PGA: Pressure gradient acceleration; HVI: Horizontal viscous acceleration; and VVI: Vertical viscous acceleration.

The discussion here focuses solely on the meridional component of the momentum equation, which is correlated with zonal velocities. By considering the Coriolis acceleration term in the meridional direction ($\mathrm{COR_y} = \mathrm{fu}$, where f is Coriolis parameter and u is zonal velocity), the pattern of the $\mathrm{COR_y}$ could be used to represent the pattern of cross-shelf circulation in the zonal direction across the continental slope of the Sahul Shelf north of the Aru Islands. A positive Coriolis term was indicative of eastward currents, while a negative Coriolis term was indicative of westward currents.

Reference Case. In the WRT case, it was observed that, in the meridional direction, Ekman balance was dominant within the upper 20 m of the surface layer along with Section A, as indicated by the relatively high VVI and COR terms with opposite directions (Figure 11). This correlated well with the westward offshore surface currents across the continental slope connecting the Aru Islands and Papua Island, as shown in Figure 8a. Meanwhile, a geostrophic balance was dominant in the interior, as indicated by the relatively high PGA and COR terms with opposite directions, correlated with eastward currents (Figures 9a and 11). Over the continental shelf (4.8°S/134.4°–136.5°E), the nonlinear advection ($\mathrm{ADV_y}$) term also contributed significantly to the momentum balance (Figure 11), suggesting that the significantly high $\mathrm{ADV_y}$ term was related to nonlinear interactions between tidal flow and topography, which could subsequently influence the mean flows around this area. Figure 11 shows that the $\mathrm{ADV_y}$ term is mostly balanced by the PGA term, with this balance being much lower in the WR case.

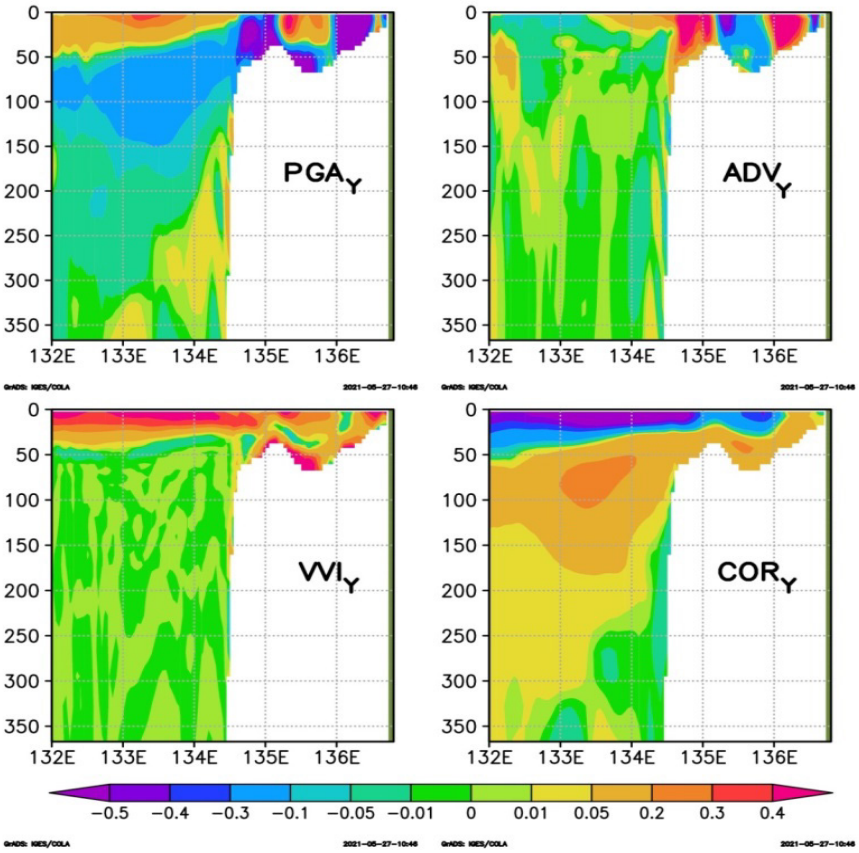

Figure 11. Momentum components in the meridional direction in Section A in the WRT case monthly averaged for the July 2004 period (28 days) (x 10^{-3} ms^{-2}).

Comparison Between the River Inclusion and Exclusion Cases in Simulations. The WRT and WT cases produced similar results for the area north of the Aru Islands. However, the two simulations differed in the magnitude of each momentum component (Figure 12). In general, river runoff enhanced vertical density stratification and weakened the vertical eddy viscosity coefficient. Consequently, interfacial stress in the surface water in the WRT case was weakened, and the surface Ekman depth was reduced. As a result, reduced interfacial stress in the WRT case enhanced the VVI term, as observed in the upper layer (<15 m depth), where most of the wind's frictional energy was trapped in the so-called plume layer. The VVI term in the meridional direction being higher in the WRT case than in the WT case was indicated by positive values ($\Delta VVI_y > 0$) (Figures 11 and 12), while the reverse patterns were generally true. Considerable modifications to the PGA_y and ADV_y terms were also found in the upper layer, with changes comparable to changes in the VVI_y

term (Figures 11 and 12). The results showed that changes to the VVI_y, PGA_y, and ADV_y terms in the WRT case were balanced by a considerably higher COR_y term ($\Delta COR < 0$, Figures 11 and 12); this, in turn, indicated stronger offshore surface currents in the zonal direction. It was found that the stronger offshore surface currents across the slope were compensated by relatively stronger onshore subsurface currents over the continental slope, whereas dominant geostrophic balance was identified. Here (just below the plume layer), it was observed that—in contrast to the plume layer—the lower interfacial stress induced by stronger stratification (due to river runoff) reduced the viscosity force (which was mostly indicated by $\Delta VVI < 0$). As a result, the stronger negative PGF ($\Delta PGF < 0$) and lower VVI terms in the WRT case were balanced by a relatively higher COR term ($\Delta COR > 0$). As already discussed in Section 4 (Figures 8a and b), the stronger COR term above the slope in the WRT case indicated stronger cross-shelf circulation and stronger upwelling, which induced a colder SST than in the WT case.

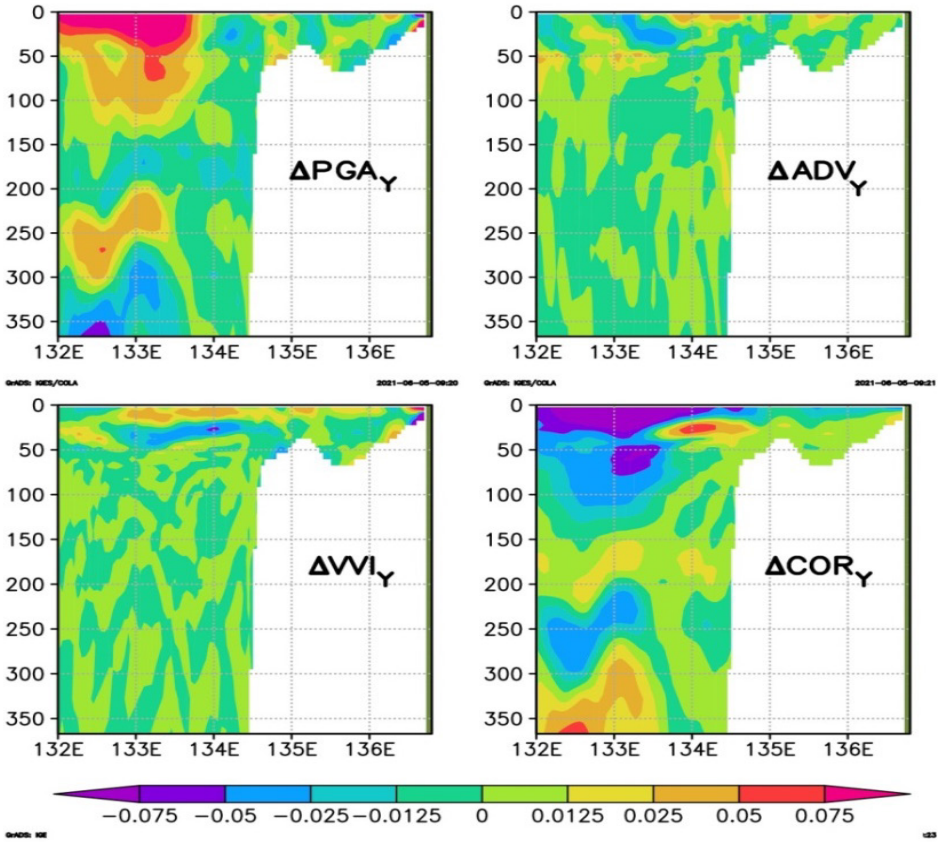

Figure 12. Difference of momentum components in the meridional direction in Section A between the WT and WRT cases (WRT-WT), monthly averaged for the July 2004 period (28 days) (x 10^{-3} ms^{-2}).

CONCLUSION

HAMSOM could reproduce upwelling events north of the Aru Islands, as indicated by the vertical velocity, relatively lower SST, and higher SSS. The model suggested that the surface waters were strongly influenced by South Pacific Subtropical Water (SPSW), which is characterized by relatively high salinity (approx. 35). However, this salinity was too salty compared to the observation. It was suggested that this condition was due to the relatively small vertical turbulent coefficient applied in the simulation. However, the simulation generally could still explain the hydrodynamic conditions around the research area, as found in the observation.

The study also suggested that tidal forcing significantly reduced salinity within the internal salinity maximum layer in the northern Arafura Sea. This lower salinity was indicative of relatively stronger tidal mixing, considering the origin of these waters, which occurred mostly around the Halmahera Sea. Tidal mixing also reduced the thermocline temperature. Furthermore, when river runoff and tidal forcing were applied together in the simulation, river runoff was also found to induce significantly lower salinity in the internal salinity maximum layer. In contrast, when tidal forcing was excluded from the simulation, river runoff contributed relatively little to reducing subsurface salinity.

Momentum analysis found that the upwelling around this area was driven mainly by Ekman surface transport, as induced by southeasterly winds. Ekman layer was revealed in the upper 20 m depth and below that subsurface layer belonged to the undercurrent system as also suggested by Kämpf (2016), which was called the eastern ITF in this study. It was also found that river runoff resulted in stronger cross circulation and thus increased upwelling during the southeast monsoon. The cross circulation was related to the enhanced vertical viscous forces at the surface layer, as indicated by stratification being stronger in the river simulation (the WRT case) than in the no-river simulation (the WT case). Similarly, stronger upwelling was also found to result in SST and SSS north of the Aru Islands being lower in the WRT case than in the WT case. Considering the surface waters' origin in the Sahul Shelf and the internal salinity maximum layer, it was concluded that the lower surface salinity in this area was influenced not only by river runoff along the western coast of Papua Island but also by the salinity of the internal salinity maximum layer being lower in the WRT than in the WT case. The lower temperature of the internal salinity maximum layer advected from Halmahera to the northern Arafura Sea in the WRT case was also suggested contributing to the reduced SST north of the Aru Islands.

The improvement of mixing parameterization of the model applied in this study needs to be conducted in future research so that the hydrodynamic conditions in this study area could be more clearly understood. Then, the upwelling variability and its mechanism are other concerns to be investigated in the future study because the Arafura Sea and its surrounding are strongly influenced by the ENSO and IOD events (Iskandar, 2010).

ACKNOWLEDGMENT

Authors would thank Deutscher Akademischer Austauschdienst (DAAD), Deutsches Klimarechen zentrum (DKRZ) and National Research and Innovation Agency (Indonesian: Badan Riset dan Inovasi Nasional, BRIN) for their financial and logistical supports.

REFERENCES

Allen, J. S., Newberger, P. A., & Federiuk, J. (1995). Upwelling circulation on the Oregon continental shelf. Part 1: Response to idealized forcing. *Journal of Physical Oceanography*, *25*, 1843-1866. https://doi.org/10.1175/1520-0485(1995)025<1843:UCOTOC>2.0.CO;2

Alongi, D. M., Edyvane, K., do Ceu Guterres, M. O., Pranowo, W. S., Wirasantosa, S., & Wasson, R.(2011). *Biophysical profile of the Arafura and Timor Seas, Report prepared for the Arafura Timor Seas Ecosystem Action (ATSEA) Program.* United Nations Development Programme (UNDP) & Global Environmental Facility (GEF). https://iwlearn.net/iw-projects/3522/reports/biophysical-profile-of-the-arafura-and-timor-seas

Atmadipoera, A. S., Almatin, A. A., Zuraida, R., & Permanawati, Y. (2020). Seasonal upwelling in the Northern Arafura Sea from multidatasets in 2017. *Pertanika Journal of Science & Technology*, *28*(4), 1487-1515. https://doi.org/10.47836/pjst.28.4.19

Backhaus, J. O. (1985). A three-dimensional model for the simulations of shelf sea dynamics. *Deutsche Hydrographische Zeitschrift*, *38*, 165-187. https://doi.org/10.1007/BF02328975

Basit, A. (2019). *Upwelling and related processes in the Banda and Northern Arafura Seas* (Doctoral dissertation). Hamburg University, Germany. Staats-und Universitätsbibliothek Hamburg Carl von Ossietzky. https://ediss.sub.uni-hamburg.de/handle/ediss/6182

Caldwell, P. C., Merrifield, M. A., & Thompson, P. R. (2015). *Sea level measured by tide gauges from global oceans - The joint archive for sea level holdings* (NCEI Accession No. 0019568, Version 5.5). NOAA National Centers for Environmental Information.

Döll, P., Kaspar, F., & Lehner, B. (2003). A global hydrological model for deriving water availability indicators: Model tuning and validation. *Journal of Hydrology*, *270*, 105-134. https://doi.org/10.1016/S0022-1694(02)00283-4

Egbert, G. D., & Erofeeva, S. Y. (2002). Efficient inverse modeling of barotropic ocean tides. *Journal of Atmosphericand Oceanic Technology*, *l19*, 183-204. https://doi.org/10.1175/1520-0426(2002)019<0183:EIMOBO>2.0.CO;2

Egbert, G. D., Bennett, A. F., & Foreman, M. G. G. (1994). TOPEX/POSEIDON tides estimated using a global inverse model. *Journal of Geophysical Research*, *99*, 24821-24852. https://doi.org/10.1029/94JC01894

Gan, J., Li, L., Wang, D., & Guo, X. (2009). Interaction of a river plume with coastal upwelling in the northeastern South China Sea. *Continental Shelf Research*, *29*, 728-740. https://doi.org/10.1016/j.csr.2008.12.002

Gieskes, W. W. C., Kraay, G. W., Nontji, A., Setiapermana, D., & Sutomo. (1990). Monsoonal differences in primary production in the eastern Banda Sea (Indonesia). *Netherlands Journal of Sea Research*, *25*(4), 473-483. https://doi.org/10.1016/0077-7579(90)90071-N

Good, S. A., Martin, M. J., & Rayner, N. A. (2013). EN4: Quality controlled ocean temperature and salinity profiles and monthly objective analyses with uncertainty estimates. *Journal of Geophysical Research: Oceans*, *118*, 6704- 6716. https://doi.org/10.1002/2013JC009067

Gordon, A. L. (2005). Oceanography of the Indonesian seas and their throughflow. *Oceanography*, *18*, 14-27. https://doi.org/10.5670/oceanog.2005.01

Gordon, A. L., Ffield, A., & Ilahude, A. G. (1994). Thermocline of the Flores and Banda seas. *Journal of Geophysical Research: Oceans*, *99*(C9), 18235-18242. https://doi.org/10.1029/94JC01434

Gordon, A. L., Sprintall, J., Van Aken, H. M., Susanto, R. D., Wijffels, S., Molcard, R., Ffield, A., Pranowo, W., & Wirasantosa, S. (2010). The Indonesian throughflow during 2004-2006 as observed by the INSTANT program. *Dynamics of Atmosphere and Oceans*, *50*, 115-128. https://doi.org/10.1016/j.dynatmoce.2009.12.002

Gordon, A. L., Susanto, R. D., Ffield, A., Huber, B. A., Pranowo, W., & Wirasantosa, S. (2008). Makassar strait throughflow 2004 to 2006. *Geophysical Research Letters*, *35*(24), Article L24605. https://doi.org/10.1029/2008GL036372

Ilahude, A. G., Komar, & Mardanis. (1990). On the hydrology and productivity of the northern Arafura Sea. *Netherlands Journal of Sea Research*, *25*(4), 573-582. https://doi.org/10.1016/0077-7579(90)90079-V

Iskandar, I. (2010). Seasonal and interannual patterns of sea surface temperature in Banda Sea as revealed by self-organizing map. *Continental Shelf Research*, *30*(9), 1136-1148. https://doi.org/10.1016/j.csr.2010.03.003

Jungclaus, J. H., Botzet, M., Haak, H., Keenlyside, N., Luo, J. J., Latif, M., Marotzke, J., Mikolajewicz, U., & Roeckner, E. (2006). Ocean circulation and tropical variability in the coupled model ECHAM5/MPI-OM. *Journal of Climate*, *19*, 3952-3972. https://doi.org/10.1175/JCLI3827.1

Kalnay, E., Kanamitsu, M., Kistler, R., Collins, W., Deaven, D., Gandin, L., Iredell, M., Saha, S., White, G., Woollen, J., & Zhu, Y. (1996). The NCEP/NCAR 40-year reanalysis project. *Bulletin of the American Meteorological Society*, *77*(3), 437-472. https://doi.org/10.1175/1520-0477(1996)077<0437:TNYRP>2.0.CO;2

Kämpf, J. (2016). On the majestic seasonal upwelling system of the Arafura Sea. *Journal of Geophysical Research: Oceans*, *121*, 1218-1228. https://doi.org/10.1002/2015JC011197

Kida, S., & Richards K. J. (2009). Seasonal sea surface temperature variability in the Indonesian Seas. *Journal of Geophysical Research: Oceans*, *114*, Article C06016. https://doi.org/10.1029/2008JC005150

Kochergin, V. P. (1987). Three-dimensional prognostic models. In N. S. Heaps (Ed.), *Three-dimensional Coastal Ocean Models* (pp. 201-208). American Geophysical Union Publishing.

Koch-Larrouy, A., Atmadipoera, A., Van Beek, P., Madec, G., Aucan, J., Lyard, F., Grelet, J., & Souhaut, M. (2015). Estimates of tidal mixing in the Indonesian archipelago from multidisciplinary INDOMIX in-situ data. *Deep Sea Research Part I: Oceanographic Research Papers*, *106*, 136-153. https://doi.org/10.1016/j.dsr.2015.09.007

Koch-Larrouy, A., Madec, G., Bouruet-Aubertot, P., Gerkema, T., Bessières, L., & Molcard, R. (2007). On the transformation of Pacific water into Indonesian throughflow water by internal tidal mixing. *Geophysical Research Letters*, *34*(4), 1-6. http://dx.doi.org/10.1029/ 2006GL028405

Lentz, S. J. (2001). The influence of stratification on the wind-driven cross-shelf circulation over the north Carolina shelf. *Journal of Physical Oceanography*, *23*, 2749-2760. https://doi.org/10.1175/1520-0485(2001)031<2749:TIOSOT>2.0.CO;2

Marsland, S. J., Haak, H., Jungclaus, J. H., Latif, M., & Röske, F. (2003). The Max-Planck-Institute global Ocean/sea ice model with orthogonal curvilinear coordinates. *Ocean Modelling*, *5*, 91-127. https://doi.org/10.1016/S1463-5003(02)00015-X

Mayer, B., & Damm, P. E. (2012). The Makassar Strait throughflow and its jet. *Journal of Geophysical Research: Oceans, 117*(C7), Article C07020. https://doi.org/10.1029/2011JC007809

Mayer, B., Damm, P. E., Pohlmann, T., & Rizal, S. (2010). What is driving the ITF? An illumination of the Indonesian throughflow with a numerical nested model system. *Dynamics of Atmospheres and Oceans*, *50*, 301-312. https://doi.org/10.1016/j.dynatmoce.2010.03.002

Monterey, G., & Levitus, S. (1997). *Seasonal variability of mixed layer depth for the World Ocean, NOAA Atlas NESDIS 14*. U.S. Government Publishing Office. https://doi.org/10.1029/2005GL022463

Nagai, T., & Hibiya, T. (2015). Internal tides and associated vertical mixing in the Indonesian Archipelago. *Journal of Geophysical Research: Oceans*, *120*(5), 3373-3390. https://doi.org/10.1002/ 2014JC010592

Nagai, T., Hibiya, T., & Bouruet-Aubertot, P. (2017). Nonhydrostatic simulations of tide-induced mixing in the Halmahera Sea: A possible role in the transformation of the Indonesian throughflow waters. *Journal of Geophysical Research: Oceans*, *122*(11), 8933-8943. https://doi.org/10.1002/2017JC013381

Nagai, T., Hibiya, T., & Syamsudin, F. (2021). Direct estimates of turbulent mixing in the Indonesian archipelago and its role in the transformation of the Indonesian throughflow waters. *Geophysical Research Letters*, *48*(6), Article e2020GL091731. https://doi.org/10.1029/2020gl091731

Nugroho, D., Koch-Larrouy, A., Gaspar, P., Lyard, F., Reffray, G., &Tranchant, B. (2018). Modelling explicit tides in the Indonesian seas: An important process for surface sea water properties. *Marine Pollution Bulletin*, *131*, 7-18. https://doi.org/10.1016/j.marpolbul.2017.06.033

Pohlmann, T. (1996a). Calculating the development of the thermal vertical stratification in the north sea with a three-dimensional baroclinic circulation model. *Continental Shelf Research*, *16*(2)*,* 163-194. https://doi.org/10.1016/0278-4343(95)00018-V

Pohlmann, T. (1996b). Calculating the annual cycle of the vertical eddy viscosity in the North Sea with a three-dimensional baroclinic shelf sea circulation model*. Continental Shelf Research*, *16*(2), 147-161. https://doi.org/10.1016/0278-4343(94)E0037-M

Pohlmann, T. (2006). A meso-scale model of the central and southern North Sea: Consequences of an improved resolution. *Continental Shelf Research*, *26*, 2367-2385. https://doi.org/10.1016/j.csr.2006.06.011

Purwandana, A., Cuypers, Y., Bouruet-Aubertot, P., Nagai, T., Hibiya, T., & Atmadipoera, A. S. (2020). Spatial structure of turbulent mixing inferred from historical CTD datasets in the Indonesian seas. *Progress in Oceanography*, *184*, Article 102312. https://doi.org/10.1016/j.pocean.2020.102312

Ray, R., & Susanto, R. D. (2016). Tidal mixing signatures in the Indonesian seas from high-resolution sea surface temperature data. *Geophysical Research Letters, 43*, 8115-8123. https://doi.org/10.1002/2016gl069485

Sprintall, J., Gordon, A. L., Koch-Larrouy, A., Lee, T., Potemra, J. T., Pujiana, K., & Wijffels, S. (2014). The Indonesian Seas and their impact on the Coupled Ocean Climate System. *Nature Geoscience*, *7,* 487-492. https://doi.org/10.1038/NGEO2188

Sprintall, J., Gordon, A. L., Wijffels, S. E., Feng, M., Hu, S., Koch-Larrouy, A., Phillips, H., Nugroho, D., Napitu, A., Pujiana, K., & Susanto, R. D. (2019). Detecting change in the Indonesian seas. *Frontiers in Marine Science*, *6*, Article 257. https://doi.org/10.3389/fmars.2019.00257

Sprintall, J., Wijffels, S., Gordon, A. L., Field, A., Molcard, R., Susanto, R. D., Soesilo, I., Sopa-heluwakan, J., Surachman, Y., & van Aken H. M. (2004). INSTANT: New international array to measure the Indonesian throughflow. *Eos, Transactions American Geophysical Union*, *85*(39)*,* 369-376.

Wetsteyn, F. J., Ilahude, A. G., & Baars, M. A. (1990). Nutrient distribution in the upper 300 m of the eastern Banda Sea and northern Arafura Sea during and after the upwelling season, August 1984 and February 1985. *Netherlands Journal of Sea Research*, *25*(4), 449-464. https://doi.org/10.1016/0077-7579(90)90069-S

Wyrtki, K. (1961). *Scientific results of marine investigations of the South China Sea and the Gulf of Thailand 1959-1961, Naga Report vol. 2*. The University of California press. https://doi.org/10.1017/S0025315400054370

Zijlstra, J. J., Baars, M. A., Tijssen, S. B., Wetsteyn, F. J., Witte, J. I. J., Ilahude, A. G., & Hadikusama. (1990). Monsoonal effects on the hydrography of the upper saters (<300 M) of the eastern Banda sea and northern Arafura sea, with specila reference to vertical transport process. *Netherlands Journal of Sea Research*, *25*(4), 431-447. https://doi.org/10.1016/0077-7579(90)90068-R

SUPPLEMENTARY DATA

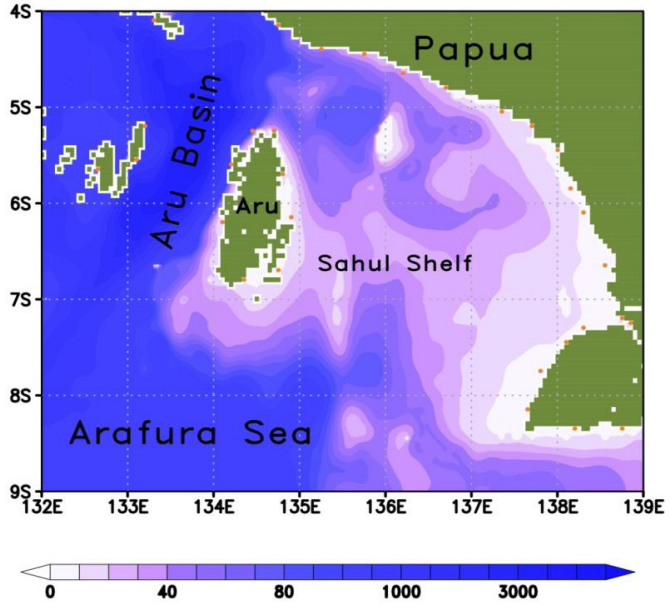

Figure A1. Bathymetry of the Sahul Shelf in meters. The solid orange circles along the coastline represent the river locations.

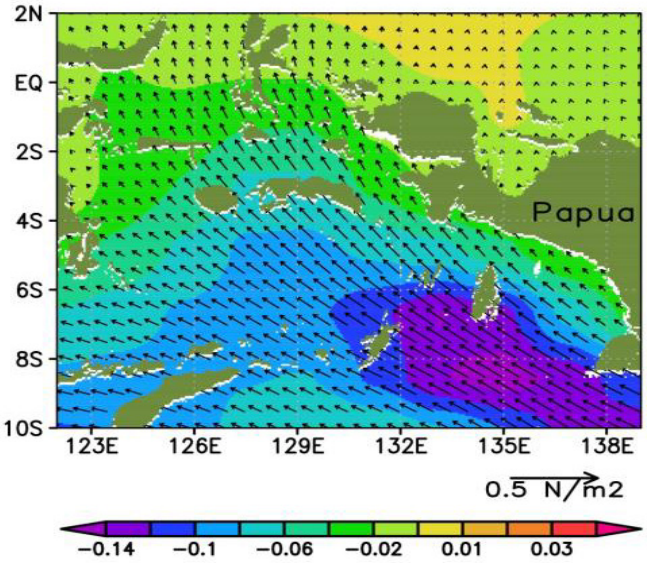

Figure A2. Horizontal distribution of average wind stress vectors (Nm^{-2}) and their magnitudes (background) derived from NCEP data, monthly averaged for the July 2004 period (28 days).

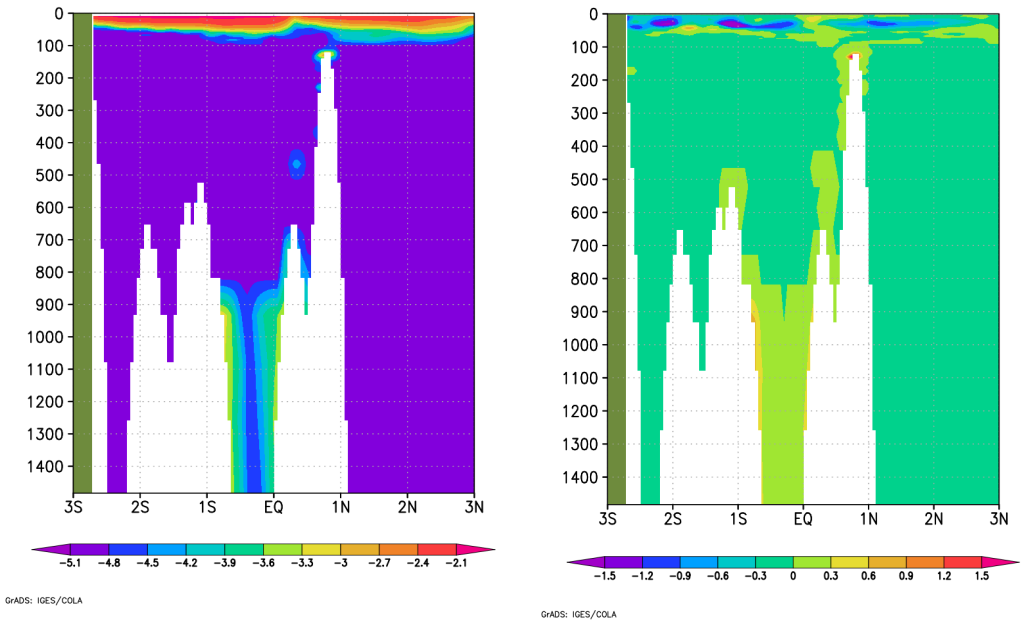

Figure A3. Vertical turbulent viscosity coefficient (log10 A_v, m^2/s) for the WRT case and the difference of vertical turbulent viscosity coefficients (x 10^{-3} m^2/s) between the WRT and WR (left) cases (b) in Section B of the Halmahera Sea (see also Figure 1), monthly averaged for the July 2004 period (28 days).

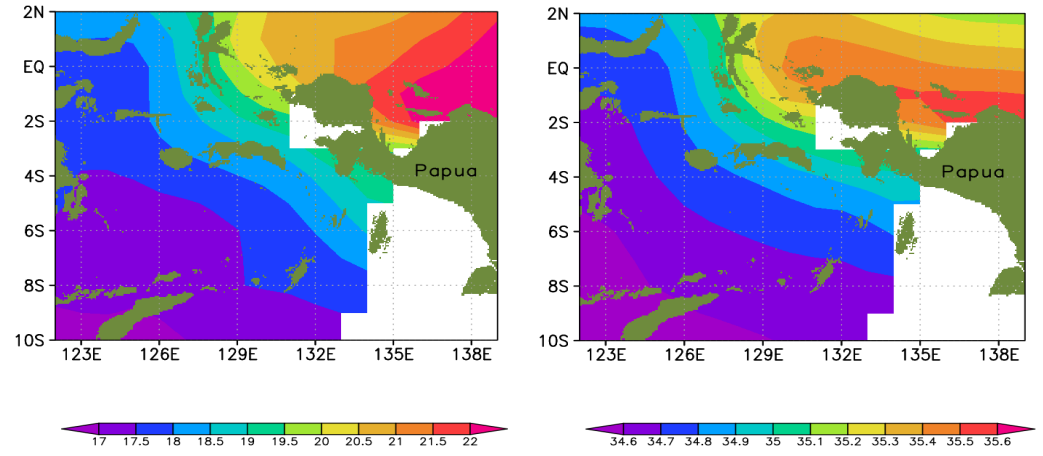

(a) (b)

Figure A4. Monthly averages of subsurface temperature (°C) (a) and subsurface salinity (b) at a depth of 130 m derived from EN4 data, monthly averaged for the July 2004 period (28 days).

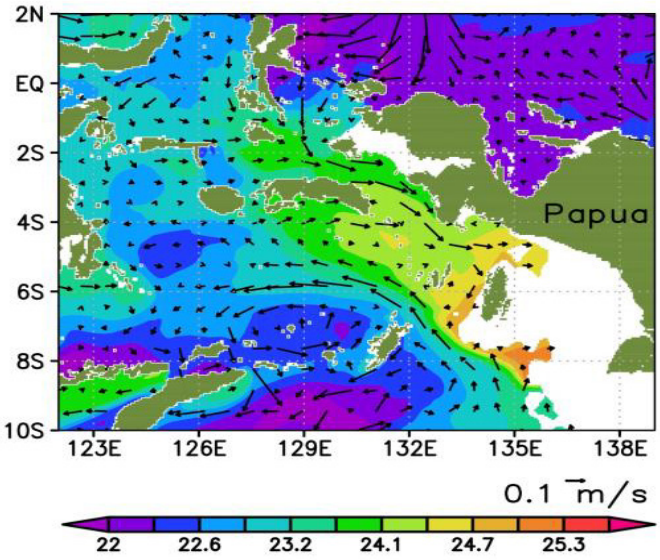

Figure A5. Subsurface currents overlaid by horizontal distribution of density (+1000 kg/m^3) at approx. 60 m depth, monthly averaged for the July 2004 period (28 days) in the WRT case.

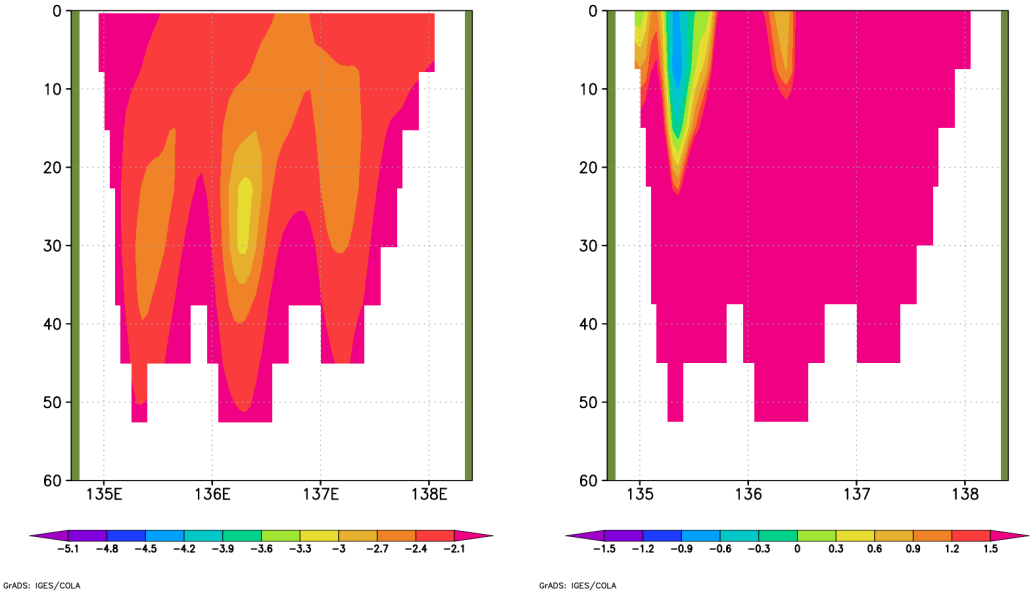

(a) (b)

Figure A6. Vertical turbulent viscosity coefficient (log10 A_v, m^2/s) for the WRT case and the difference of vertical turbulent viscosity coefficients (x 10^{-3} m^2/s) between the WRT and WR (left) cases (b) in Section C of the Sahul Shelf (see also Figure 1), monthly averaged for the July 2004 period (28 days).

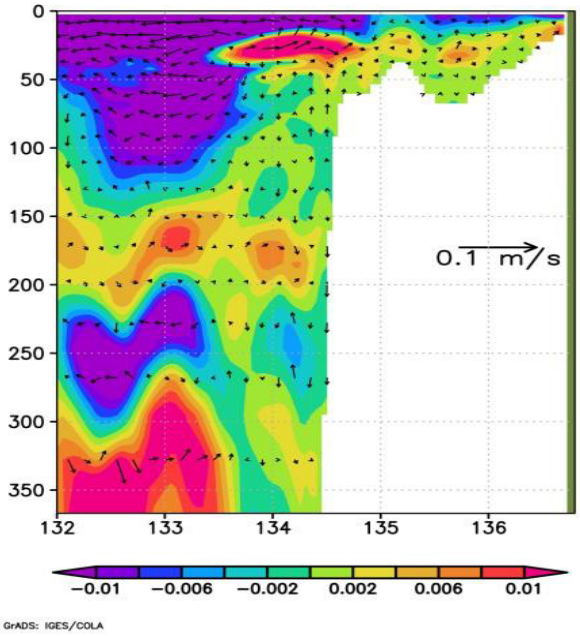

Figure A7. Difference of u-velocities between the WRT and WT cases (u_{WRT}-u_{WT}), overlaid by u-w velocity difference (uw_{WRT}- uw_{WT}), monthly averaged for the July 2004 period (28 days)